J. Fluid Mech. (1986), vol. 162, pp. 339–363
Printed in Great Britain

The structure of the vorticity field in turbulent channel flow. Part 2. Study of ensemble-averaged fields

By JOHN KIM AND PARVIZ MOIN
NASA Ames Research Center, Moffett Field, California 94035

(Received 15 October 1984 and in revised form 26 July 1985)

Several conditional-sampling techniques are applied to data bases generated by large-eddy and direct numerical simulations. It is shown that the bursting process is associated with well-organized vortical structures inclined at about 45° to the wall. These vortical structures are identified by examining the vortex lines of three-dimensional instantaneous and ensemble-averaged vorticity fields. Two distinct horseshoe-shaped vortical structures corresponding to the sweep and ejection events are detected. These vortical structures are associated with high Reynolds shear stress and hence make a significant contribution to turbulent-energy production.

1. Introduction

In Moin & Kim (1985, hereinafter referred to as Part 1), an investigation of the existence of horseshoe (or hairpin) vortex structures in turbulent channel flow was reported in which a data base generated by the large-eddy simulation technique was used. It was shown that, in a large portion of the flow, the distribution of the inclination angle of vorticity vectors attains its maximum at about 45° to the wall. Two-point correlations of velocity and vorticity fluctuations along lines inclined at 45° and 135° to the flow direction provided strong evidence for the existence of vortical structures inclined at 45° to the wall. In addition to these statistical analyses, the vorticity vectors and vortex lines of instantaneous three-dimensional vorticity fields also indicated the presence of horseshoe-vortex structures. It was shown that these structures are generated from deformation (or roll-up) of sheets of transverse vorticity.

In the present paper, we further study the structure of the vorticity field in turbulent channel flow, using various conditional-sampling techniques. The objective of this work is to identify the vortical structures associated with the *bursting process* in the wall-bounded turbulent flows. The bursting process is composed of a sequence of quasi-cyclic events that occur in turbulent flows; it is responsible for about 70 % of the *total* turbulence production in boundary layers (see Kim, Kline & Reynolds 1971; Kline 1978). Our aim is to determine whether the organized structures associated with the bursting process are indeed horseshoe vortices, as was first hypothesized by Kline *et al.* (1967). The dependence of the ensemble-averaged vortical structures on the detection criteria, and the question of whether the ensemble-averaged structure is an artifact of the ensemble-averaging process are also examined.

The same data base as used in Part 1 is used here. The data base was obtained by large-eddy simulation of a fully developed turbulent channel flow (Moin & Kim

1982) for a Reynolds number of 13800, based on the centreline velocity and channel half-width. The calculations were carried out with 516096 grid points ($64 \times 63 \times 128$, in x, y, z). The grid spacings in the streamwise and spanwise directions were $\Delta x^+ \approx 62$ and $\Delta z^+ \approx 15$ in wall units.† Non-uniform meshes were used in the normal direction, and the first mesh point away from the wall was at $y^+ \approx 1.8$. Three-dimensional velocity and pressure fields were stored at widely separated flow times. This data base has also been used in previous investigations of the organized turbulence structures (Kim 1983, 1985; Moin 1984) and has provided information complementing experimental studies of the coherent motions in turbulent flows. In order to explore the effect of computational grid resolution and the subgrid-scale motions on the detected structures, a direct numerical simulation is performed in which all important turbulence scales are resolved (i.e. with no subgrid-scale modelling). These calculations are carried out with about 4×10^6 grid points at a relatively low Reynolds number ($Re = 3200$). The direct-simulation results are compared with the results obtained from the large-eddy simulation.

In §2, a brief description of several conditional-sampling techniques is presented. The results obtained by applying those techniques to the aforementioned data base are given in §3. Discussion of these results is presented in §4, and a summary is provided in §5. Finally, the results from the fine-mesh computation (direct simulation) are given in the Appendix.

2. Conditional-sampling techniques

The VITA (variable-interval time-averaging) sampling technique of Blackwelder & Kaplan (1976) has been widely used in the past to investigate turbulence structures associated with the bursting process. Previous investigations of the structures of wall-layer turbulence using a variant of the VITA sampling technique indicated that the bursting process (on the average) is associated with a pair of counter-rotating streamwise vortices (Kim 1983, 1985). Whether these streamwise vortices are indeed the 'legs' of a horseshoe vortex structure could not be established because only the streamwise component of the ensemble-averaged vorticity field was examined in two-dimensional cross-stream planes. To address this question, the three-dimensional vorticity *vector* field obtained from the VISA (variable-interval space-averaging) sampling technique (Kim 1983, 1985) is used in the present work. The VISA technique is essentially the same as VITA, except that VISA produces a spatial structure instead of a temporal one. The exact definition of this conditional-sampling technique is given in table 1, along with the other techniques used in this work. However, as is discussed in more detail in the next section, detection by VISA is not triggered by the passage of horseshoe vortices (see also Falco 1980). This is because sampling in VITA (especially the later version of Chen & Blackwelder 1978) is basically triggered by a sweeping event, that is, a region of high-speed fluid moving toward the wall causing a local acceleration near the wall (Corino & Brodkey 1969). In order to have a detection scheme triggered by the ejection of low-speed fluid from the wall region (ejection event), which is likely to be associated with horseshoe vortices, the location of the detection point was moved away from the wall to $y^+ = 100$, 200 and 300, corresponding to $y/\delta = 0.15$, 0.31 and 0.47 respectively. In addition, the

---

† The superscript + indicates a non-dimensional quantity scaled by the wall variables; e.g. $y^+ = yu_\tau/\nu$, where ν is the kinematic viscosity and $u_\tau = (\tau_w/\rho)^{\frac{1}{2}}$ is the wall-shear velocity.

VISA	$\hat{u}(x,y,z,t_0,L)=\frac{1}{L}\int_{x-\frac{1}{2}L}^{x+\frac{1}{2}L} u(\xi,y,z,t_0)\,\mathrm{d}\xi$ $\widehat{\mathrm{var}}=\widehat{u^2}-\hat{u}^2$ $D(\xi)=1$, if $\widehat{\mathrm{var}}>ku^2_{\mathrm{rms}}$ and $\partial u/\partial x<0$, $=0$, otherwise $\langle u(x,y,z,t_0)\rangle=\frac{1}{N}\sum_{j=1}^{N} u(x+\xi_j,y,z,t_0)$ where $k=1.2$, $L^+=500$ and the detection point at $y^+=21$
VISA-1	Same as VISA except that: $D(\xi)=1$, if $\widehat{\mathrm{var}}>ku^2_{\mathrm{rms}}$ and $\partial u/\partial x>0$ Detection point at $y^+=100$ ($y/\delta=0.15$)
VISA-2	Same as VISA-1 except $y^+=200$ ($y/\delta=0.31$)
VISA-3	Same as VISA-1 except $y^+=300$ ($y/\delta=0.47$)
QD-2	$D(\xi)=1$, if $u'<0$, $v'>0$, and $u'v'/\overline{u'v'}>10$, $=0$, otherwise $\langle u(x,y,z,t_0)\rangle=\frac{1}{N}\sum_{j=1}^{N} u(x+\xi_j,y,z,t_0)$ Detection point at $y^+=100$
QD-4	$D(\xi)=1$, if $u'>0$, $v'<0$, and $u'v'/\overline{u'v'}>10$, $=0$, otherwise $\langle u(x,y,z,t_0)\rangle=\frac{1}{N}\sum_{j=1}^{N} u(x+\xi_j,y,z,t_0)$ Detection point at $y^+=21$
QD-A	Same as QD-2 except that: $D(\xi)=1$, if $u'<0$, $v'>0$, and $0<u'v'/\overline{u'v'}<1$, $=0$, otherwise
QD-B	Same as QD-2 except that: $D(x)=1$, if $u'<0$, $v'>0$, and $1<u'v'/\overline{u'v'}<2$, $=0$, otherwise

TABLE 1. Conditional-sampling techniques

detection function was set such that it only detects a local deceleration,† which is normally associated with the ejection event. These techniques are referred to as VISA-1, -2 and -3 in table 1.

Anticipating that the induced velocities of horseshoe vortices would produce high Reynolds shear stress, the quadrant analysis (Willmarth & Lu 1972; Wallace, Eckelmann & Brodkey 1972; Alfredsson & Johansson 1984) is also applied to the same

---

† Note that the terms acceleration and deceleration are used to describe the velocity measured by a fixed probe in space. Corresponding velocity distribution in the streamwise direction would be a negative gradient of the streamwise velocity for the acceleration and a positive gradient for the deceleration.

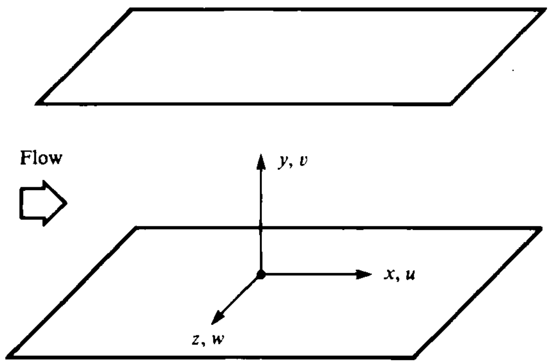

FIGURE 1. Coordinate system in channel.

data base. Of particular interest are the second ($u' < 0, v' > 0$) and the fourth ($u' > 0$, $v' < 0$) quadrants, which make positive contributions to turbulent energy production. With this technique, vortical structures associated with the sweep and ejection events can be separated. These techniques will be referred to as QD-2 and QD-4 in the remainder of this paper. In an attempt to measure the contribution of the detected vortical structures to the Reynolds shear stress, different sizes of threshold intervals are added to the quadrant analysis. This is in contrast to the 'hole' technique of Lu & Willmarth (1973), which selects events associated with the Reynolds stress larger than a threshold value. These techniques are referred to as QD-A and QD-B in table 1.

Ensemble-averaged structures obtained using these conditional-sampling techniques will depend on the detection criteria of each technique. The educed structures, therefore, are the 'average' structures associated with the particular events that the conditional-sampling techniques are designed to detect: for example, structures detected by QD-2 are associated with the ejection event, whereas structures detected by QD-4 are associated with the sweep event. Many different structures occur in turbulent flows, and a special technique can be devised to detect a particular structure. Important structures are those that play a significant role in the dynamics of the flow.

All the results presented in the following section are obtained from ensemble averages of more than 1000 events. Some of the results (VISA) are averaged over more than 3000 events. The coordinate system used in this paper is shown in figure 1. Here, x, y and z represent the streamwise, normal (to the wall), and spanwise directions respectively; u, v and w denote the velocity components along x, y and z respectively. The origin of the streamwise coordinate, $x = 0$, and the spanwise coordinate, $z = 0$, corresponds to the location of the detection point, and y is measured from the wall. The lengthscales are non-dimensionalized by the wall parameters, and, for the Reynolds number considered here, the channel half-width corresponds to $\delta^+ \approx 640$.

3. Ensemble-averaged vortical structures

The vortical structures are identified by tracing vortex lines in three-dimensional space $\boldsymbol{x}$. The lines are defined by

$$\frac{\mathrm{d}\boldsymbol{x}}{\mathrm{d}s} = \frac{\boldsymbol{\omega}}{|\boldsymbol{\omega}|}, \tag{1}$$

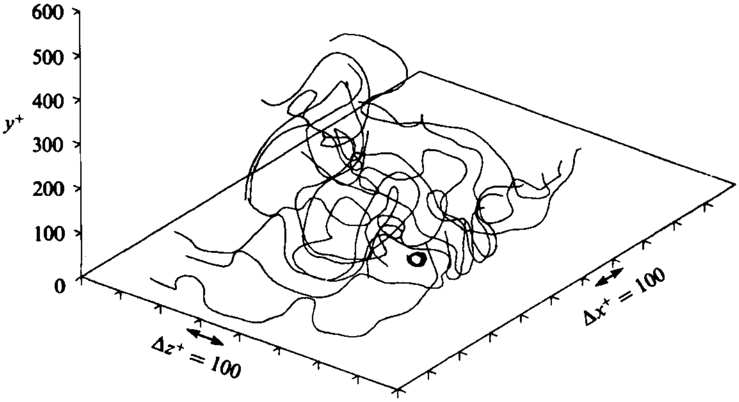

FIGURE 2. Randomly chosen instantaneous vortex lines in a turbulent flow.

where s is the distance along the vortex line and ω is the vorticity vector. In Part 1 instantaneous vortex lines in turbulent channel flow illustrated the three-dimensional structure of the horseshoe vortices. In this section we consider vortex lines of averaged vorticity fields obtained from the various conditional-sampling techniques† described in §2. These vortex lines show the shape of the ensemble-averaged vortical structures. Some quantitative information, such as velocity and vorticity signatures and magnitudes, for the case of VISA, can be found in Kim (1983). Other quantitative information concerning the quadrant analysis and comparisons with the experimental data are presented in the Appendix.

In figure 2, several randomly chosen vortex lines in an instantaneous computed vorticity field are shown. The chaotic nature of the flow is quite apparent, but several horseshoe-shaped vortex lines can be identified. As will be shown below, some of the conditional-sampling techniques are triggered by horseshoe vortices, and the resulting ensemble-averaged patterns display a pronounced horseshoe (or hairpin) shape. In some techniques other structures, as well as the horseshoe vortices, trigger sampling, and the ensemble-averaged patterns show a similar but weaker structure.

The vortex lines of the ensemble-averaged vorticity field obtained using VISA are shown in figure 3. Only the vortex lines near the detection point ($x = 0$, $z = 0$) are shown in the figure; the vortex lines that approach $y^+ \approx 55$ as $z \rightarrow \pm\infty$ for several x-locations upstream and downstream of the detection point are shown in figure 3(*a*); those that approach $y^+ \approx 106$ for the same streamwise locations are shown in figure 3(*b*). Note that the *time-averaged* flow field contains only the spanwise vorticity component, and the planar vortex sheets associated with this field are parallel to the (x, z)-plane. Any departure from these planar vortex sheets indicates the presence of organized vortical structures‡ that survived a particular ensemble-averaging process. Figure 3(*a*) shows the existence of weak vortical structures downstream of the detection point ($x > 0$). The ensemble-averaged field contains appreciable streamwise and normal vorticity components (their time-averaged values are zero),

---

† Note that, for all the conditional-sampling techniques used in the present work, the vorticity of an ensemble-averaged velocity field is the same as the ensemble-averaged vorticity field. See the definitions of the ensemble averages in table 1.

‡ The term 'vortical structure' is used here to denote an organized structure that contains an appreciable perturbation vorticity from the mean flow. The connection between this vortical structure and a true vortex associated with a revolving motion is discussed in the Appendix.

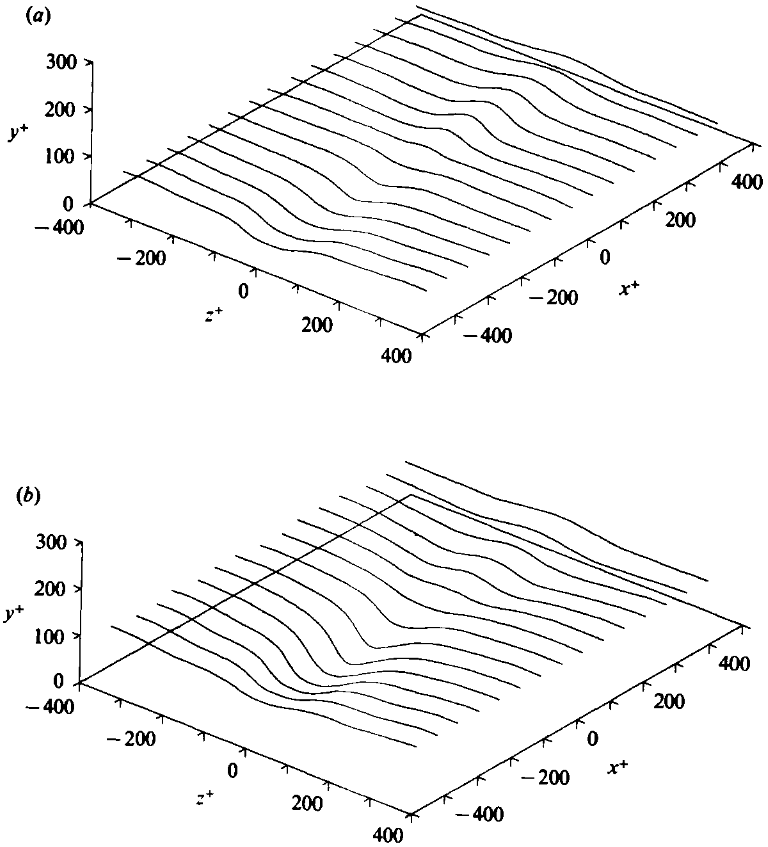

FIGURE 3. Vortex lines of VISA ensemble in the vicinity of the detection point: (a) lines that approach $y^+ \approx 55$ as $z \rightarrow \infty$; (b) lines that approach $y^+ \approx 106$ as $z \rightarrow \infty$.

but their magnitudes are relatively small compared with that of the spanwise component. Upstream of the detection point, a different vortical structure is noticeable (especially at higher y^+ locations, figure 3b). The apexes of its vortex lines are located upstream of their legs and closer to the wall. The induced fluid motion from this vortical structure corresponds to the sweep event, whereas the induced motion owing to the downstream vortical structure corresponds to the ejection of fluid away from the wall. For a probe fixed in space, the passage of these structures would first register positive normal velocity followed in time by negative velocity; this is in agreement with the experimental measurements using the VITA technique (Blackwelder & Kaplan 1976; Alfredsson & Johansson 1984).

It should be pointed out that the *ensemble*-averaged structures are smeared out relative to the instantaneous ones, because the instantaneous structures appear randomly in time and space with jitter in their size, shape and strength (induced velocity). Therefore these ensemble-averaged structures are not confined to a compact region in space and should not be considered as representative of instantaneous structures. However, the vortex lines of the averaged structure are indicative of the shapes of the detected instantaneous structures. A comparison between instantaneous detected structures and ensemble-averaged structures will be made in the next section when we discuss the results from QD-2.

The perturbation ensemble-averaged vorticity field is obtained by subtracting the

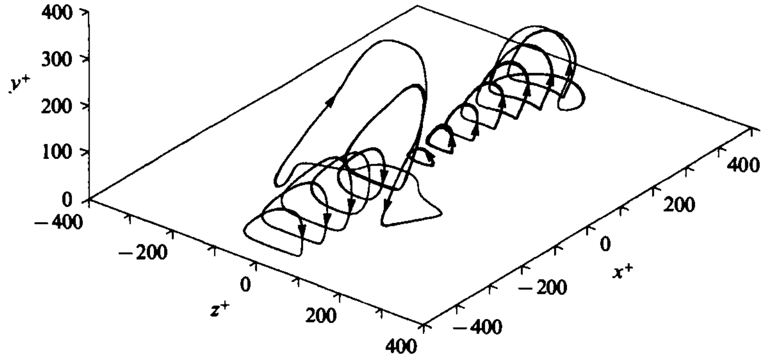

FIGURE 4. Vortex lines corresponding to the perturbation vorticity field. The lines shown are those that pass through the point of maximum pertubation vorticity for a given streamwise location.

mean component of vorticity from the ensemble-averaged field. The vortex lines corresponding to this perturbation field are shown in figure 4. The lines shown are those that pass through the point of the maximum perturbation vorticity for a given streamwise location; that is, the starting point for the integration of (1) was the point of maximum perturbation vorticity in the (y, z)-plane for a given x. These vortex lines display ring-like loops. The direction of the vorticity is indicated by arrows. Distinct groups of loops exist upstream and downstream of the detection point corresponding to the sweep and ejection motions. The presence upstream of the detection point of *vorticity* of sign opposite to the mean vorticity, and one downstream with the same sign is in agreement with the measurements of Falco (1980). The ensemble-averaged vorticity field can be represented by straight vortex lines in the spanwise direction (mean vorticity) superposed with vortex loops (perturbation). This is similar to the initial condition used by Leonard (1980) for the numerical simulation of a turbulent spot, in which ring vortices were added to the mean vorticity.

Figure 5 displays the vortex lines of the ensemble-averaged field obtained using VISA-1. Recall that VISA-1 is designed to detect flow deceleration, which is normally associated with ejection of low-speed fluid away from the wall. Again, only the vortex lines near the detection point are shown. The vortex lines in figures 5 (*a–d*) approach $y^+ \approx 20$, 55, 143, and 300 respectively, as $z \rightarrow \infty$; these figures display a variation of the vortical structure as a function of the distance from the wall. Close to the wall (figure 5*a*) all the vortex lines are parallel to the spanwise direction (direction of mean vorticity thus representing an undisturbed planar vortex sheet), indicating no apparent organized structure there; a pronounced vortical structure near the detection point is shown in figure 5(*b*); the two vortical structures associated with the sweep and ejection are shown in figure 5(*c*); and, in figure 5(*d*), no vortical structure is noticeable far away from the wall. When the detection point is moved farther away from the wall ($y/\delta = 0.31$, VISA-2), these vortical structures become more pronounced, as shown in figure 6. The asymptotic y-locations of the vortex lines chosen for figures 5(*b*, *c*), and for figures 6(*a*, *b*) correspond to the locations yielding the most pronounced vortical structures for each case. To illustrate variations of the ensemble-averaged vortical structure in the y-direction, vortex lines approaching various y-locations as $z \rightarrow \infty$ for a given streamwise location are also shown in figures 6(*c*, *d*). In figure 6(*c*), the end view of the vortex lines at $x^+ \approx -190$ displays the vortical structure associated with the ejection event; the end view of the vortex

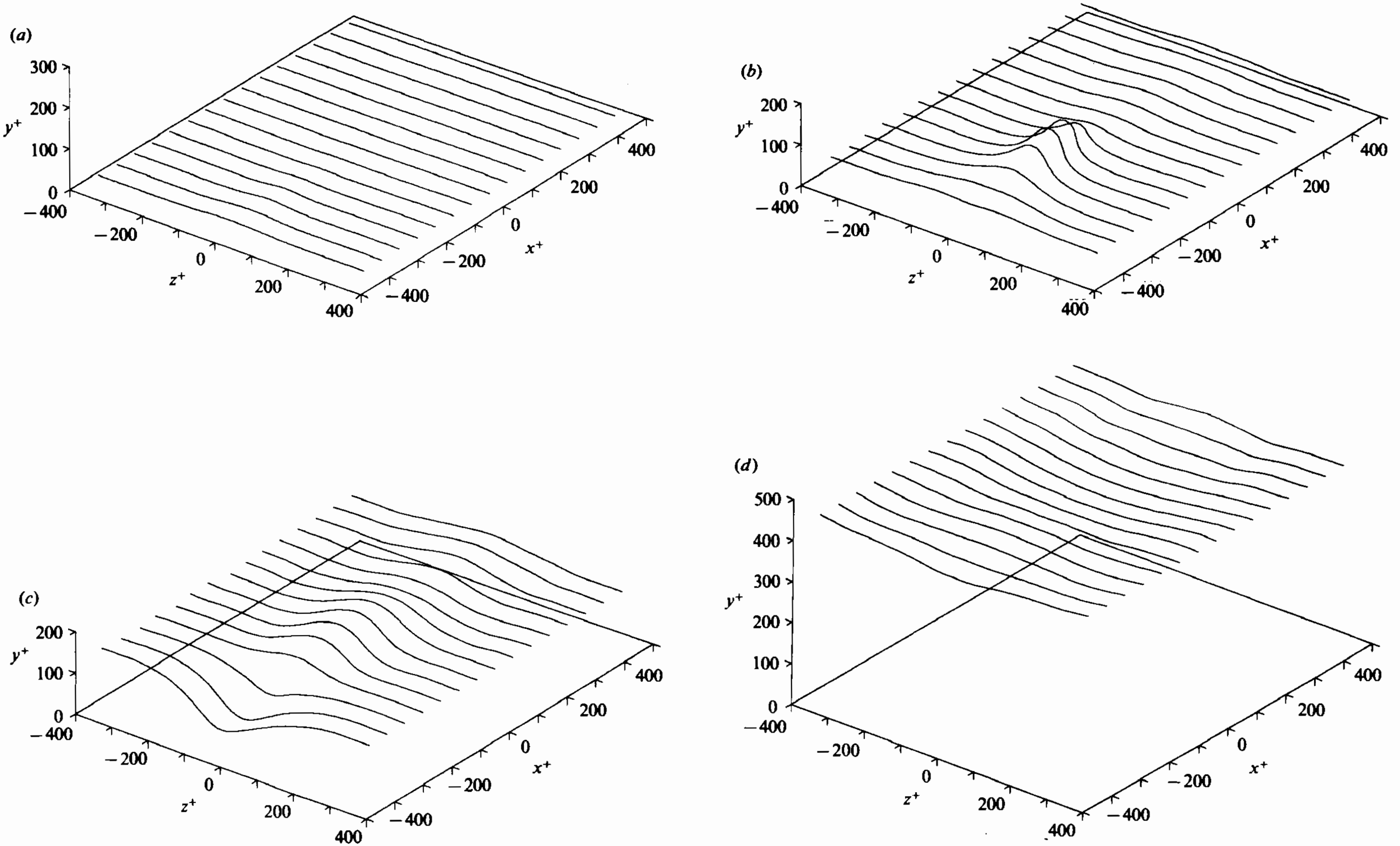

FIGURE 5. Vortex lines of VISA-1 ensemble in the vicinity of the detection point: (*a*) lines that approach $y^+ \approx 20$ as $z \rightarrow \infty$; (*b*) lines that approach $y^+ \approx 55$; (*c*) lines that approach $y^+ \approx 143$; (*d*) lines that approach $y^+ \approx 300$.

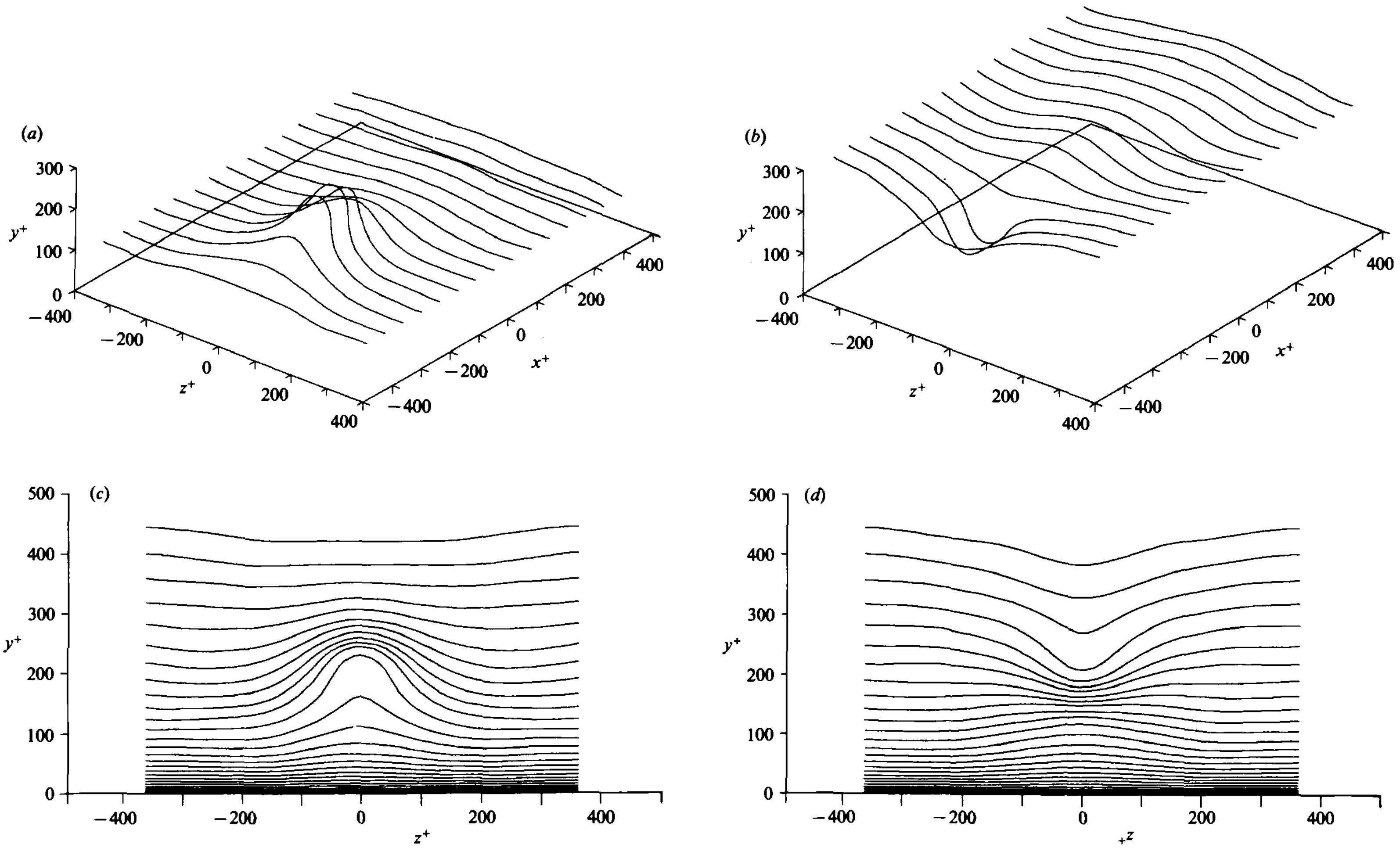

FIGURE 6. Vortex lines of VISA-2 ensemble in the vicinity of the detection point: (*a*) lines that approach $y^+ \approx 106$ as $z \rightarrow \infty$; (*b*) lines that approach $y^+ \approx 320$; (*c*) end view of the vortex lines at $x^+ \approx -190$ for several y-locations; (*d*) end view of the vortex lines at $x^+ \approx -380$.

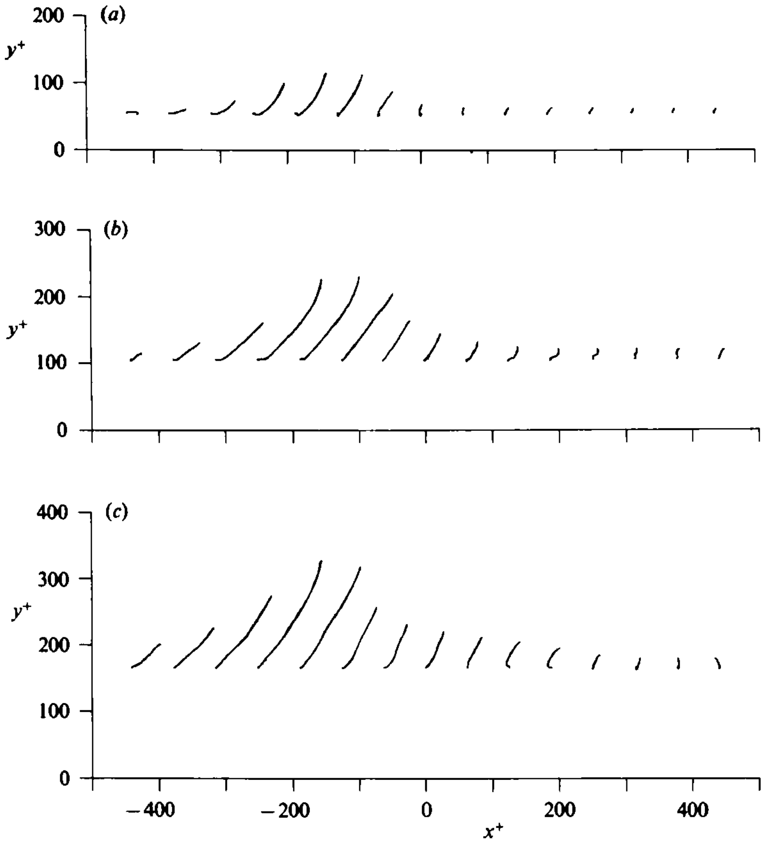

FIGURE 7. Side view of the vortex lines: (*a*) VISA-1; (*b*) VISA-2; (*c*) VISA-3.

lines at $x^+ \approx -380$ displays the vortical structure associated with the sweep event in figure 6(*d*). Placing the detection point farther away ($y/\delta = 0.47$, VISA-3) does not yield any stronger structures. Figure 7 shows the side view of the votex lines seen in figures 5(*b*) and 6(*a*) and the one obtained from VISA-3. It can be seen that these vortical structures are inclined at about 45° to the wall. Their upper portions generally are inclined at larger angles because the self-induced velocity of a curved vortex filament is largest in the region where the curvature of the filament is maximum (i.e. the tip region).

The second quadrant of the (u', v')-space, $u' < 0$ and $v' > 0$, corresponds to the ejection of low-speed fluid away from the wall. QD-2 is designed to detect such events. The vortex lines obtained from this conditional-sampling technique are shown in figure 8. Near the detection point ($x = 0$, $z = 0$), a pronounced horseshoe-shaped vortical structure is clearly discernible. The side view of the vortex lines illustrates that they are inclined at about 45° to the wall. In comparison with the previous figures obtained from the variants of VITA (figures 3–7), QD-2 results in a more pronounced vortical structure. Examination of the vortex lines at all y-locations indicates that QD-2 does not yield the structures associated with the sweep event observed in the VISA series.

In contrast to the 'hole' technique (Lu & Willmarth 1973) used in QD-2, which detects events associated with Reynolds shear stress larger than a threshold value,

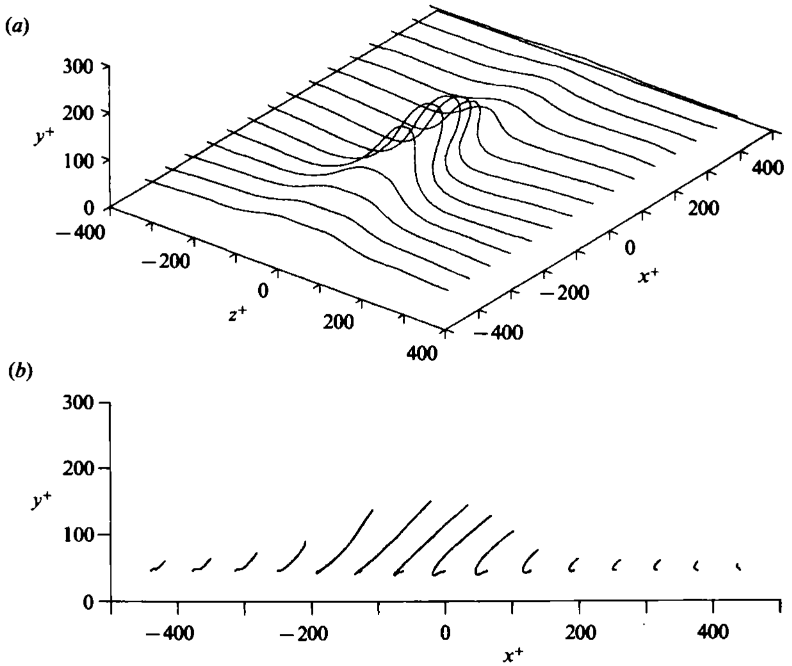

FIGURE 8. Vortex lines of QD-2 ensemble. The lines shown are those that approach $y^+ \approx 55$ as $z \rightarrow \infty$: (a) oblique view; (b) side view.

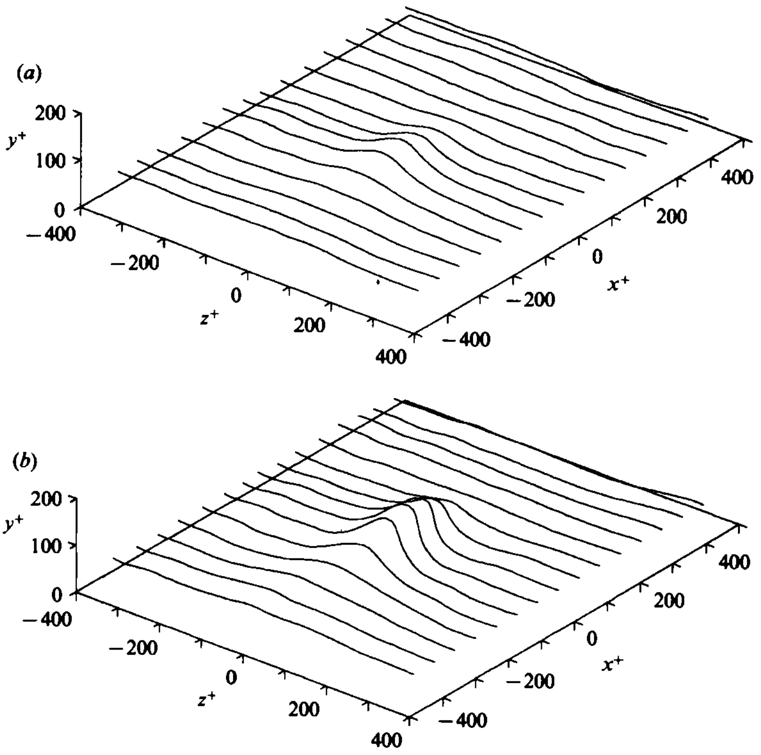

FIGURE 9. Vortex lines of (a) QD-A and (b) QD-B ensembles. The lines are those that approach $y^+ \approx 55$ as $z \rightarrow \infty$.

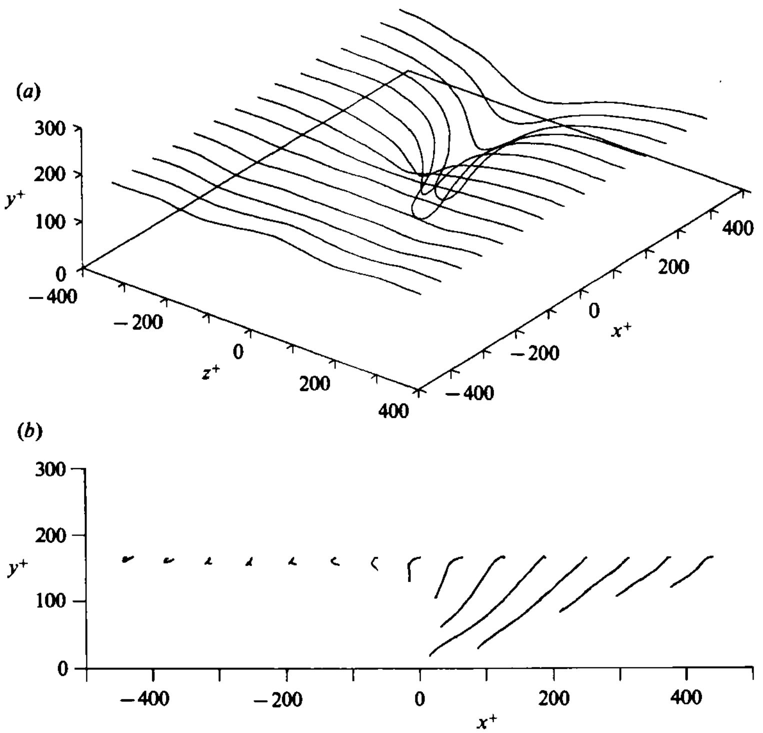

FIGURE 10. Vortex lines of QD-4 ensemble. The lines shown are those that approach $y^+ \approx 170$ as $z \rightarrow \infty$: (a) oblique view; (b) side view.

QD-A and QD-B select events associated with the Reynolds shear stress in a specified range ('window'). Figure 9 shows the results obtained from using two different window sizes. By comparing figures 8 and 9, it is clear that the stronger vortical structure (with large perturbation vorticity) is associated with the higher Reynolds shear stress – not a surprising result considering their induced motions.

As mentioned earlier in this section, the ensemble-averaged vorticity fields obtained from variants of the VITA technique (VISA, VISA-1, 2, 3) suggest that there are two distinct vortical structures associated with the sweep and ejection events. The structure obtained by QD-2 corresponds to the latter. To investigate the vortical structure directly associated with the sweep event, QD-4 is applied to the data base. The vortex lines of the ensemble-averaged vorticity field obtained using QD-4 are shown in figure 10. As anticipated from the previous results (figures 5–6), they display a pronounced vortical structure associated with the sweep event. The side view of this structure (figure 10*b*) also shows inclination of about 45° to the wall. In figure 10, we note that the spatial scales of the tip involved in the sweep event are rather small. This is consistent with Falco's (1980) observations that small scales are associated with the sweep event that directly initiates the bursting process.

4. Discussion

The ensemble-averaged vorticity fields provide strong evidence for the presence of horseshoe-shaped vortical structures during the bursting process. Two different vortical structures are identified; they are associated with the sweep and ejection

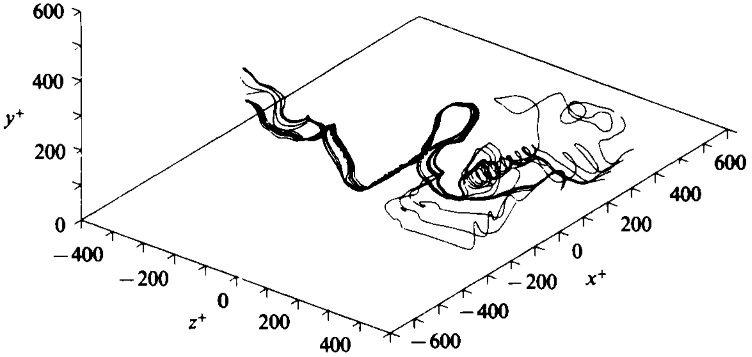

FIGURE 11. Vortex lines showing an instantaneous structure detected by QD-2.

events respectively. However, as mentioned earlier, the ensemble-averaged structures are somewhat smeared out. This problem is particularly serious for single-probe detection schemes such as those used in the present study. This is probably why the ensemble-averaged vortical structures presented in the previous section resemble Hill's spherical vortex rather than a 'true' vortex (defined as an agglomeration of vortex lines in a compact region). To investigate whether the instantaneous detected structure is a true vortex, instantaneous vorticity fields are also examined. A typical instantaneous vortex structure detected by QD-2 is shown in figure 11. More examples of detected instantaneous structures are shown in the Appendix. These figures (11, 13–15) illustrate the roll-up of vortex sheets into rods to produce horseshoe vortices and they demonstrate that the ensemble-averaging processes smear the detected structures into the bulges of vortex sheets instead of a true vortex. It is also shown in the Appendix that the legs of these detected vortices indeed induce revolving motions around themselves, thus confirming that they are true vortices. Further discussions of the nature of the detected vortical structures are given in the Appendix. It is apparent that these structures are the horseshoe vortices and not just a vortex sheet or a shear front. Although the ensemble-averaged structure is different from instantaneous structures owing to the smearing effect, it provides the averaged shape and scales of the vortical structures associated with the bursting process. In addition, since it is difficult to obtain three-dimensional, instantaneous (both quantitative and visual) information experimentally, the ensemble-averaged results allow comparison of the experimental and numerical results. Note that the ensemble-averaged vortical structures can be obtained in the laboratory with a minimum of two probes.

The measurements of Willmarth & Lu (1972) show that about 30 % of the total Reynolds shear stress at $y^+ = 30$ is due to motions in the second quadrant with local Reynolds shear stress in excess of 10 times the mean value. Recent experimental measurements by Alfredsson & Johansson (1984), as well as our numerical simulation (see Appendix), indicate a similar contribution at $y^+ = 50$. The results obtained by applying QD-2 to our data bases (figures 8, 9, 11, 13–15) show that these motions in the second quadrant are associated with horseshoe vortices. Therefore, we infer that these vortices make important contributions to the dynamics of the flow.

The cause of the formation of these vortical structures is not as clear as the evidence for their existence. This is mainly because we only have static pictures. One has to follow the development of such structures dynamically to investigate the processes by which they are created. Most likely, as pointed out in Part 1, these vortex lines are deformed from the primary vortex lines originally parallel to the spanwise direction (sheets of spanwise vorticity) by turbulent-velocity fluctuations. Whenever vortex lines are deformed by fluid motion either toward or away from the wall, the presence of shear will produce *both* the vortical structures associated with the sweep and ejection events by the vortex-stretching mechanism. This can be seen from the inviscid vorticity equations,

$$\frac{\mathrm{D}\omega_x}{\mathrm{D}t} = \omega_x\frac{\partial u}{\partial x}+\omega_y\frac{\partial u}{\partial y}+\omega_z\frac{\partial u}{\partial z}, \tag{2}$$

$$\frac{\mathrm{D}\omega_y}{\mathrm{D}t} = \omega_x\frac{\partial v}{\partial x}+\omega_y\frac{\partial v}{\partial y}+\omega_z\frac{\partial v}{\partial z}. \tag{3}$$

Consider a perturbation associated with a localized fluid motion moving away from the wall; the only non-zero terms in the mean flow are ω_z and $\partial u/\partial y$. Because of the imposed perturbation, the third term in the right-hand side of (3) will create positive and negative components of the normal vorticity in the region where $\partial v/\partial z$ exists. This in turn, through the second term in (2), will create streamwise components of both signs. The resulting vorticity field will be that of a horseshoe vortex. The formation of the vortical structure associated with the sweep event can be explained similarly by considering a localized fluid motion moving toward the wall. Thus the vortex-stretching terms provide the proper mechanism for the formation of the horseshoe vortices. The final angle formed by these stretched vortices is determined by a balance between the shearing and stretching action, which is described in Part 1.

The stretching process just described and the observation that some of the vortical structures are formed far away from the wall region leads us to the conjecture that these structures exist in all shear flows irrespective of the presence of a wall. This structure may play a less important role in other flows. For the wall-bounded shear flow considered here, the importance of horseshoe vortices is marked by their significant contribution to Reynolds shear stress, and hence to turbulent-energy production.

The ensemble-averaged streamwise velocity profiles associated with the vortical structures are shown in figure 12. The dashed line represents the time-averaged mean velocity, and the solid circles denote the ensemble-averaged profile from QD-4 (associated with the sweep event); the open circles denote the profiles obtained by using QD-2 (associated with the ejection event). Both profiles are obtained at $x^+ \approx 120$ downstream of the detection point, and they show pronounced excess and defect in the streamwise velocity associated with the sweep and ejection events respectively.

The educed structures presented in this paper are obtained from the ensemble-average fields. These results, therefore, represent an *average* shape of the unsteady vortical structures in turbulent channel flow. An instantaneous structure is not as symmetric and smooth as the ensemble-averaged one. In fact it can be argued that the educed structure is totally an artifice of an ensemble-averaging process. For example, ensemble-averaging can yield a *pair* of counter-rotating vortices as the dominant structures associated with a given event, if the conditional-sampling technique detects (with equal probability) a single isolated vortex of one sign to the right of the detection point and (at a different time) a vortex of opposite sign to the left. However, the instantaneous structure illustrated in figure 11 (and many other instantaneous pictures examined) revealed that this is not the case.

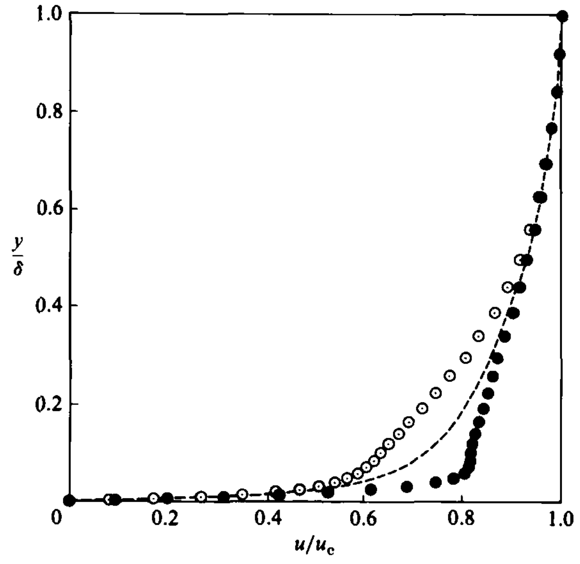

FIGURE 12. Mean and ensemble-averaged streamwise velocity profiles: ○, QD-2; ●, QD-4; ----, mean.

All the results presented so far were obtained using the data base generated from the large-eddy simulation of Moin & Kim (1982). In that simulation, the large-scale flow field was computed explicitly from the filtered Navier–Stokes equations and the small-scale field motions were simulated through an eddy-viscosity model. The grid spacing of that simulation was too coarse ($\Delta x^+ \approx 62$, and $\Delta z^+ \approx 15$) to resolve some of the observed structures at their correct scales. For example, although the calculations did produce the high- and low-speed wall-layer streaks, their mean spacing was about twice the commonly accepted value. To examine the effect of the coarse-grid resolution and the subgrid-scale model on the turbulence structures, a direct simulation with a very fine mesh at a lower Reynolds number was carried out. These results, which are presented in the Appendix, verify all the features of the vortical structures presented in this paper using the large-eddy-simulation data base.

5. Summary and conclusions

In order to investigate the organized vortical structures associated with the bursting process, several conditional-sampling techniques are applied to a data base generated by computation of turbulent channel flow. The vortical structures are identified by examining vortex lines of the three-dimensional, ensemble-averaged vorticity fields. These ensemble-averaged vortical structures display the general shape of well-organized horseshoe vortices. Examinations of instantaneous structures suggest that these vortical structures are indeed vortices associated with revolving motions. VISA, which is adapted from the VITA technique (Blackwelder & Kaplan 1976) to obtain a spatial rather than temporal structure, does not yield pronounced vortical structures. Several variants of the VITA techniques are used in the present work. It is found that there exist two distinct horseshoe-shaped vortical structures associated with the bursting event: one associated with the ejection event and the other with the sweep event.

The QD-2 and QD-4 averaging techniques, which directly sample the ejection (the second quadrant in the (u', v')-space) and sweep events (the fourth quadrant) respectively, indicate the presence of horseshoe vortices. The ensemble-averaged vortical structure has generally the same characteristics as the instantaneous structures, but they are smeared out by the averaging process, thus producing bulges of vortex sheets, whereas the instantaneous structures are identified as vortex filaments with revolving motions about their axes. The conditional-sampling criteria are triggered by high Reynolds shear stress indicating that these structures make a significant contribution to turbulent-energy production.

It was argued that the vortex-stretching mechanism alone can produce horseshoe-shaped vortices regardless of the presence of a wall. This supports the conjecture (Theodorsen 1952) that horseshoe vortices are characteristic of all shear flows (not just the wall-bounded shear flows with which they are commonly associated). For the wall-bounded shear flows considered here, these are the dominant structures in the sense that they survive the ensemble-averaging process and are associated with high Reynolds shear stress.

The authors are grateful to Drs A. Leonard, R. D. Moser and R. S. Rogallo for helpful discussions during the course of this work.

Appendix. Results from direct numerical simulation

The data base used in the main text was generated from a large-eddy simulation in which only the large-scale motions are computed directly from the Navier–Stokes equation and the small-scale motions are modelled by a subgrid-scale motion. This data base has been used in the past to identify the organized structures in turbulent flows. Although it has been shown (Moin & Kim 1982; Kim 1983) that virtually all features of this data base are in good agreement with experimental data, some quantitative structural information, such as the streak spacing in the wall region, was not consistent with experimental results. This raised some questions regarding the effects of the grid resolution and the subgrid-scale model on the computed turbulence structures. To address these questions unequivocally, a direct numerical simulation of the turbulent channel flow is performed. The computation is carried out with 3 962 880 grid points (192 × 129 × 160, in x, y, z) for a Reynolds number of 3200, based on the centreline velocity and channel half-width (180 based on the wall shear velocity). The grid spacings in the streamwise and spanwise directions are $\Delta x^+ \approx 12$, and $\Delta z^+ \approx 7$ in wall units. Non-uniform meshes are used in the normal direction, the first mesh point away from the wall is at $y^+ \approx 0.05$, and the maximum spacing (at the centreline of the channel) is about 4.4 in wall units. The streamwise and spanwise extent of the computational box are respectively about 2300 and 1150 in wall units. A fully spectral method – Fourier series in the streamwise and spanwise directions and Chebychev polynomial expansion in the normal direction – is employed in this direct simulation, in contrast to the large-eddy simulation, where a second-order finite-difference method was used in the normal direction. This provides additional accuracy in the normal direction over that of the reduced grid size and Reynolds number. No subgrid-scale model is used in the computation, since it was shown (Moser & Moin 1984), and confirmed *a posteriori*, that the grid resolution is sufficiently fine to resolve the essential turbulent scales, although it is still slightly larger than the estimated Kolmogorov scale (about 2 wall units).

The computed statistics are in good agreement with the low-Reynolds-number

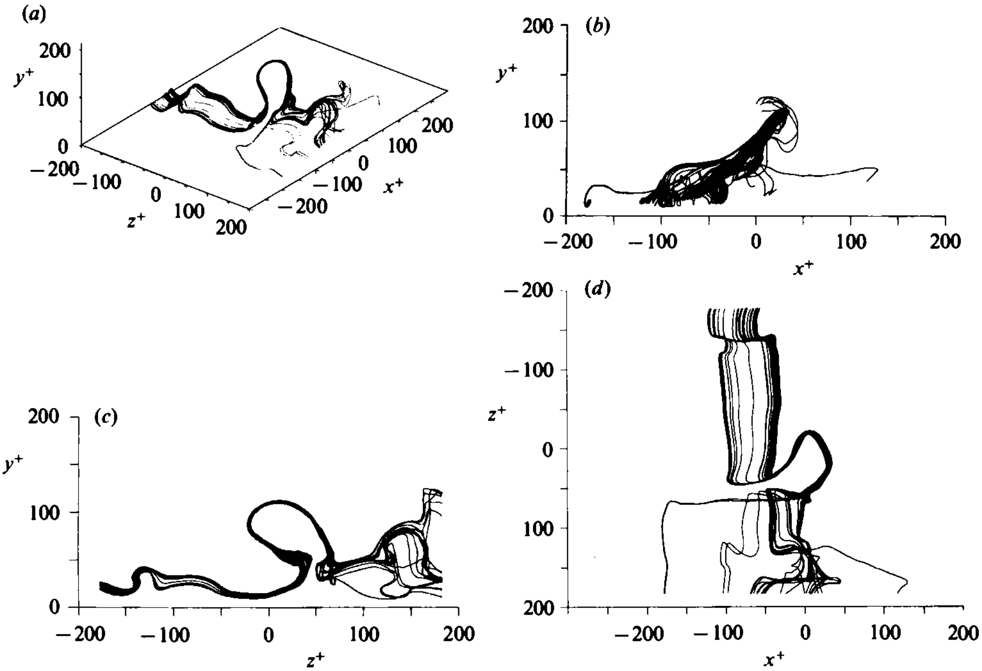

FIGURE 13. Vortex lines of an instantaneous vortical structure detected by QD-2: (a) oblique view; (b) side view; (c) end view; (d) top view.

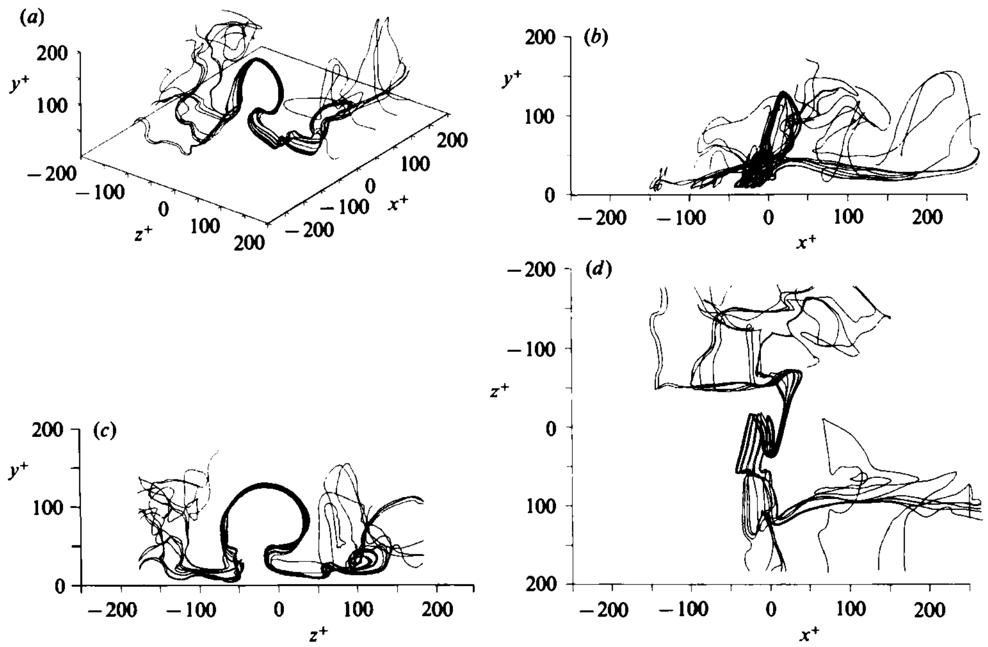

FIGURE 14. Vortex lines of an instantaneous vortical structure detected by QD-2: (a) oblique view; (b) side view; (c) end view; (d) top view.

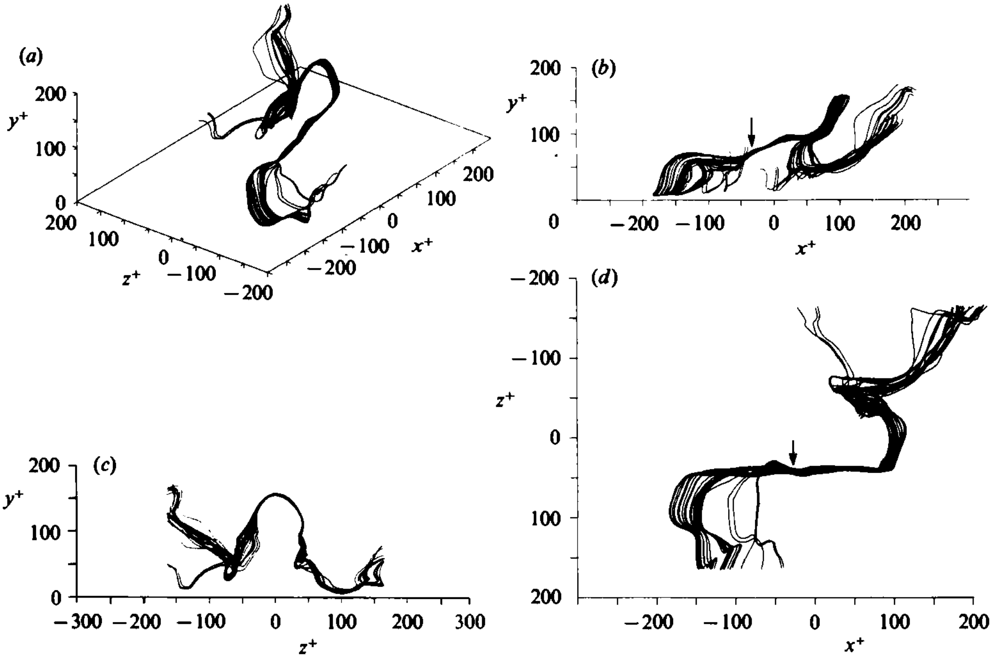

FIGURE 15. Vortex lines of an instantaneous vortical structure detected by QD-2: (*a*) oblique view; (*b*) side view; (*c*) end view; (*d*) top view.

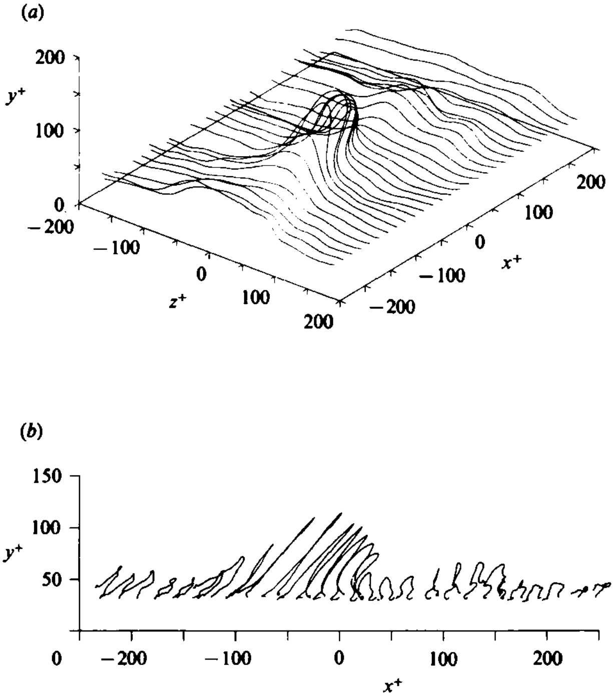

FIGURE 16. Vortex lines from QD-2. The lines shown are those that approach $y^+ \approx 33$ as $z \rightarrow \infty$: (*a*) oblique view; (*b*) side view. This figure should be compared with figure 8.

experiments of Eckelmann (1974) and Kreplin & Eckelmann (1979). In addition, the mean spacing of the wall-layer streaks, which were not captured in their proper size in the large-eddy simulation, is now in agreement with experimental results. Detailed descriptions of the numerical method and the results will be reported in the future, but some of the results relevant to the present investigation are presented here.

Comparison of the detected structures between the large-eddy and direct simulations

In figures 13–15, several snapshots of typical instantaneous structures detected by QD-2 are shown. These three cases clearly indicate that the vortex structures are formed from (i) roll-up of sheets of spanwise vorticity into vorticity rods, and (ii) vortex-stretching by the shear. The end views reveal different shapes of the detected vortices corresponding to different stages in their evolution. As pointed out in Part 1, the self-induced motion of the vortex tends to progressively convert the vortex loop into Ω-shape. Thus, the vortices in figures 13 and 14 must have evolved through the process over a longer period than the one in figure 15. It is quite feasible, as explained in Part 1, that these vortices will eventually pinch off to form vortex rings. This provides a mechanism for the generation of the vortex rings observed in turbulent boundary layers by Falco (1977, 1980).

An ensemble-averaged field is obtained from about 300 events detected by QD-2. A group of vortex lines corresponding to this field is shown in figure 16. The sample size is by no means sufficient, as the figure indicates. However, the purpose of the figure is to illustrate that the ensemble-averaged structure obtained from the direct simulation is almost the same as the one obtained from the large-eddy simulation presented in the main text. The only apparent discrepancy between the two results seems to be the scale of the vortical structure. Again, the ensemble-averaged structure demonstrates that the boundaries of the compact instantaneous vortical structures are smeared out.

In figure 17, a snapshot of a typical instantaneous structure detected by QD-4 is shown. This is the inverted horseshoe vortex associated with the sweep event (see figure 10). We note here that the detection of this structure was more difficult than that of the regular horseshoe vortex for the following reasons. First, the QD-4 events that satisfy the requirement that the local shear stress exceeds ten times the mean value occur much less frequently than the QD-2 events. Secondly, these vortical structures are located in the wall region, where significant background turbulent vorticity exists. As a result, the detection of these structures was more cumbersome than the detection of the vortical structures associated with QD-2. These are probably also the reasons that these structures have never been observed experimentally.

It is clear from these figures that the general characteristics of both instantaneously detected and ensemble-averaged structures are the same as those presented in the main text. The results from the direct simulation at a low Reynolds number are in good agreement with the available experimental results. Furthermore, except for the spatial scales of the computed eddies, all the results from the direct simulation – statistics as well as turbulence structures – are in good agreement with the results obtained from the large-eddy simulation, thus substantiating the physical realism of the large-eddy-simulation data base.

Additional details of the vortical structures

There still remains the question of whether these structures visualized by the vortex lines are 'true' vortices associated with revolving motions around their axes (a distinction should be made between vorticity and vortex when interpreting vortex

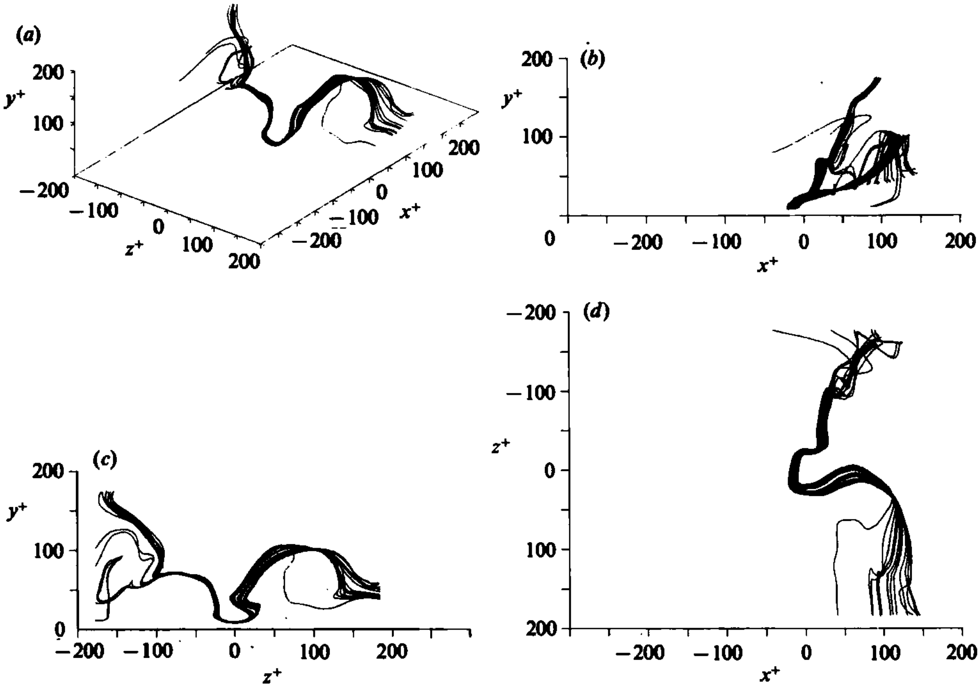

FIGURE 17. Vortex lines of an instantaneous vortical structure detected by QD-4: (*a*) oblique view; (*b*) side view; (*c*) end view; (*d*) top view.

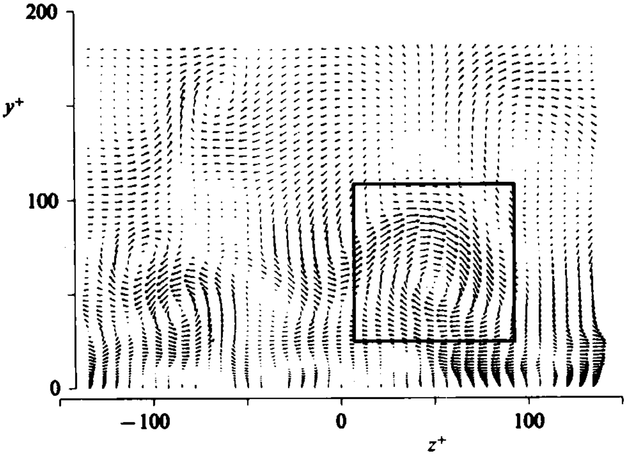

FIGURE 18. Velocity vectors in a (y, z)-plane. The streamwise location is indicated in figure 15(*b*), and the direction of the mean flow is into the figure.

lines). For this purpose, we examine the velocity fields around the axes of the 'legs' to see if there exists an observable rotating motion around them. Ideally, one should examine them in the plane perpendicular to the axes. In this case, however, one should subtract the convection velocity of the structure; otherwise the velocity in the streamwise direction is so dominant that one cannot easily detect the revolving motion in the plane. Unfortunately, this convection speed is not known (it probably

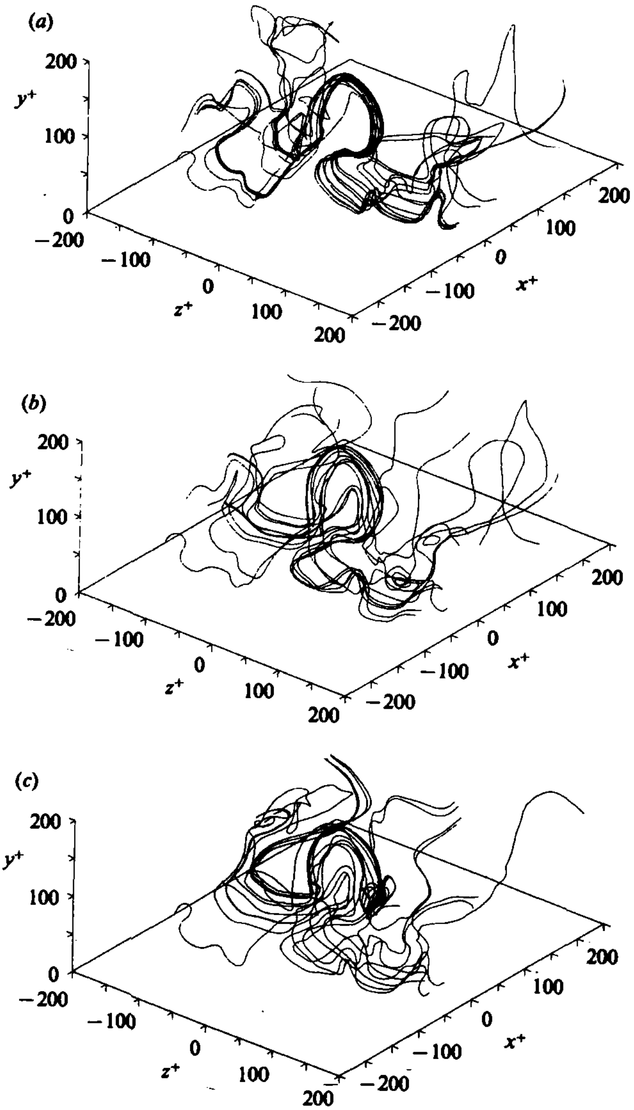

FIGURE 19. Effect of the diameter of the filament on vortical structures: (*a*) $d^+ \approx 15$; (*b*) $d^+ \approx 30$; (*c*) $d^+ \approx 40$.

varies with each individual structure) and, depending on the convection velocity subtracted, one could deduce distinctively different pictures. This problem of unknown convection velocity can be avoided if the axis of the vortex filaments is approximately perpendicular to a (y, z)-plane. The streamwise velocity does not contribute to motions in this plane, and one can simply study the normal and spanwise velocity components. For this reason the structure in figure 15 was chosen to investigate the velocity field around the axes. The velocity vectors in a (y, z)-plane, whose streamwise location is indicated by an arrow in figure 15(*b*), are shown in figure 18, and they do show revolving motion about the axis. It is apparent from this figure that the streamwise vorticity in this region contains both $\partial w/\partial y$ and $\partial v/\partial z$ – another indication that this is a vortex and not just a shear front. It should be pointed

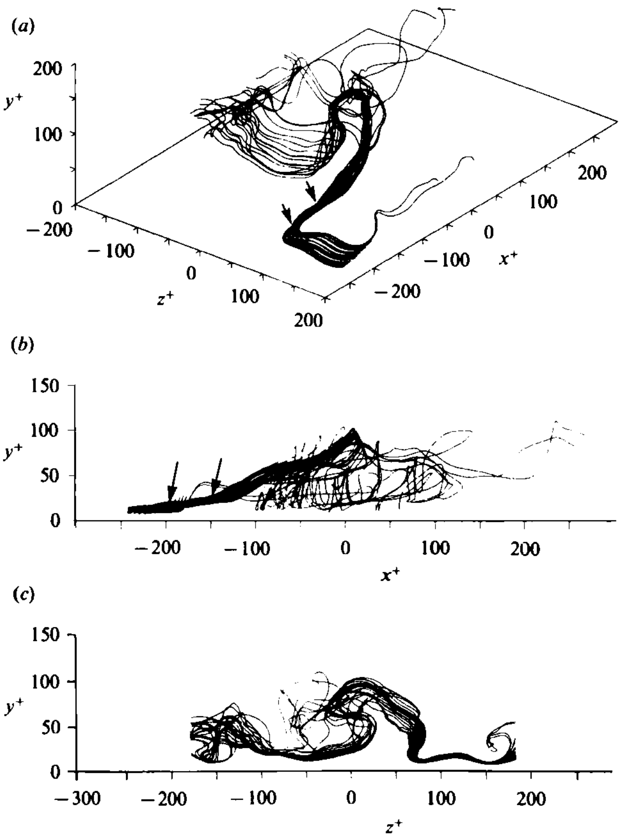

FIGURE 20. Vortex lines drawn through a streamwise vortex in the wall region: (a) oblique view; (b) side view; (c) end view.

out, however, that the sheet-like structures in figures 13–15 are not vortices. They are primarily due to the mean vorticity, and only those parts where the vortex lines coalesce into tubes represent a 'true' vortex. These figures also illustrate the roll-up of sheets of spanwise vorticity into vortices.

The vortices in the previous figures are visualized by vortex lines that pass through the neighbourhood (a small circular area) of the detection points. To investigate the effect of the diameter of these circular regions on the shape of the vortex filament, different diameters are used to initiate the vortex lines. Figure 19 shows how the identity of the vortex shown in figure 14 is being lost as the diameter increases: that is, the vortex is confined to a compact region in space.

The vortical structures that emerge from the present investigation seem to be different from some of the structures observed (or postulated) in the past, especially those of Blackwelder & Eckelmann (1979). None of the figures presented here, nor any others that we examined, show vortical structures in the wall region significantly elongated in the streamwise direction. To investigate this issue further, we explicitly searched for streamwise vortices in the wall region, $10 < y^+ < 50$, by examining streamwise vorticity magnitude and velocity-vector plots in (y, z)-planes. The streamwise vorticity component was sometimes as large as the mean spanwise vorticity at the wall. When a region with a strong streamwise vortex was found, the

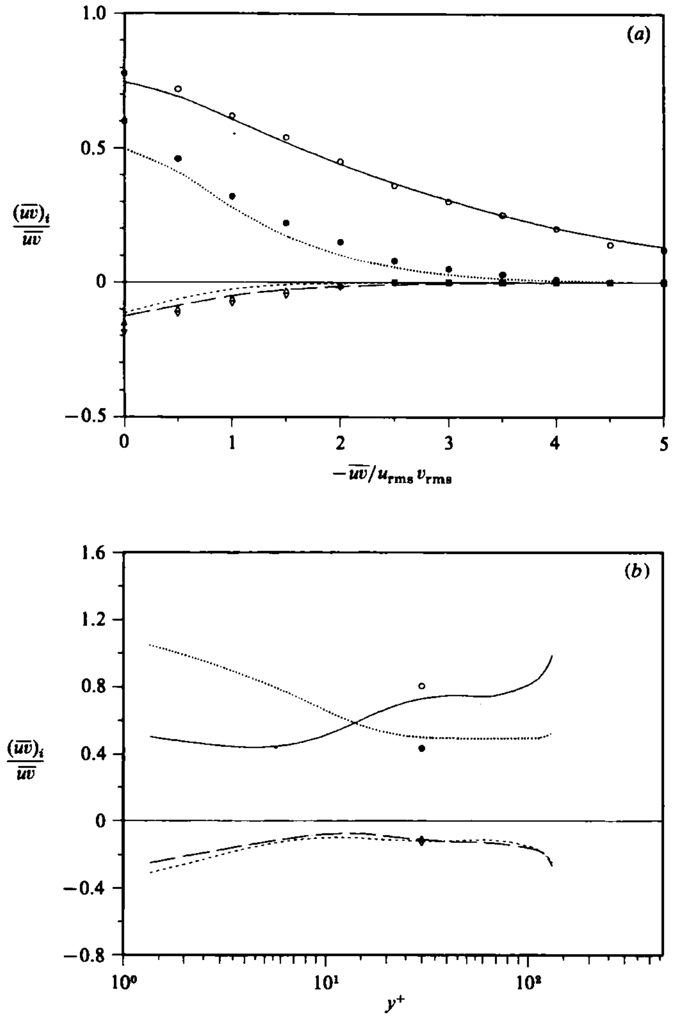

FIGURE 21. (*a*) Fractional contribution to $-\overline{uv}$ at $y^+ = 50$, normalized with the local mean Reynolds shear stress: – – – –, first; ——, second; —·—, third; - - - - - - -, fourth quadrants. Symbols represent the interpolated values from figure 3 of Alfredsson & Johansson (1984): △, first; ○, second; ▽, third; ●, fourth. (*b*) Total contribution from each quadrant normalized with the local mean Reynolds shear stress: – – – –, first; ——, second; —·—, third; - - - - - - - -, fourth quadrants. Symbols represent the experimental data of Willmarth & Lu (1972): △, first; ○, second; ▽, third; ●, fourth.

vortex lines passing through that region were traced to see if the vortex lines would lie along the streamwise direction. For all the cases examined, these regions also have a strong normal vorticity component, and the traced vortex lines form an appreciable angle with the wall. It should be pointed out that the root-mean-square values of streamwise and normal vorticity in this region are about the same (see Moin & Kim 1982; Moser & Moin 1984). Also, one should note that the presence of high- and low-speed streaks in this region inevitably produces high normal vorticity (from $\partial u/\partial z$) at their boundaries. An example of a streamwise vortex is shown in figure 20; it has the longest streamwise extent among the samples examined, but remains parallel to the wall (indicated by two arrows) for less than 100 wall units. This result is in good agreement with the observations made by Praturi & Brodkey (1978). They note that 'the streamwise vortices typically had a diameter of 50 z^+ units and length of $100x^+$. Their axes had slight y and z components'. We conclude that it is very unlikely that the vortex filaments near the wall have long streamwise extent *along* the wall (as proposed by Blackwelder & Eckelmann 1979). The same conclusion was also reached by Moser & Moin (1984), using different techniques. A possible mechanism, which can sustain long stable streaky structures without a long streamwise vortex, was given in Part 1 (Moin & Kim 1985). Note also that Blackwelder & Ecklemann did not measure the two-point correlation of streamwise vorticity to determine whether their vortices had a long extent in the streamwise direction, but relied on their velocity measurement. In a more recent paper, Blackwelder (1983) also notes that these vortices need not necessarily have long streamwise lengths.

Quadrant analysis

Fractional contributions from the four quadrants to the total Reynolds shear stress at $y^+ = 50$ are compared in figure 21 (*a*) with the experimental data of Alfredsson & Johansson (1984). The agreement with the experimental data is very good. Note that the threshold values for the fractional contributions (abscissa) are normalized by the root-mean-square values of the intensities. The correlation coefficient, $-\overline{uv}/u_{\mathrm{rms}}\,v_{\mathrm{rms}}$, at this location is about 0.4, and the threshold value of QD-2, $10\overline{uv}$, corresponds to approximately 4 on the abscissa. About 30 % of the total Reynolds stress is from the second-quadrant events with the Reynolds stress greater than 10 times the mean value. The total contribution from each quadrant as a function of y-location is shown in figure 21 (*b*) along with the experimental data of Willmarth & Lu (1972) at $y^+ = 30$. This figure clearly illustrates the dominance of the sweep event in the wall region ($y^+ < 15$) and the ejection event away from the wall consistent with the experimental results of Willmarth & Lu (1972) and Brodkey, Wallace & Eckelmann (1974). Further detailed comparisons with experimental data will be reported in the future. Here, we point out that some discrepancy exists between the experimental data of Brodkey *et al.* and the present results, especially near the wall,† but the general shape of the profiles, including the crossing location, are in good agreement.

REFERENCES

Alfredsson, P. H. & Johansson, A. V. 1984 On the detection of turbulence-generating events. *J. Fluid Mech.* **139**, 325.

Blackwelder, R. F. 1983 Analogies between transitional and turbulent boundary layers. *Phys. Fluids* **26**, 2807.

Blackwelder, R. F. & Eckelmann, H. 1979 Streamwise vortices associated with the bursting phenomenon. *J. Fluid Mech.* **94**, 577.

Blackwelder, R. F. & Kaplan, R. E. 1976 On the wall structure of the turbulent boundary layer. *J. Fluid Mech.* **76**, 89.

Brodkey, R. S., Wallace, J. M. & Eckelmann, H. 1974 Some properties of truncated turbulence signals in bounded shear flows. *J. Fluid Mech.* **63**, 209.

Chen, C. H. P. & Blackwelder, R. F. 1978 Large scale motion in a turbulent boundary layer: a study using temperature contamination. *J. Fluid Mech.* **89**, 1.

Corino, E. R. & Brodkey, R. S. 1969 A visual investigation of the wall region in turbulent flow. *J. Fluid Mech.* **37**, 1.

---

† There are differences among different experimental results reported by Wallace *et al.* (1972), Lu & Willmarth (1973), and Brodkey *et al.* (1974).

ECKELMANN, H. 1974 The structure of the viscous sublayer and the adjacent wall region in a turbulent channel flow. *J. Fluid Mech.* **65**, 439.

FALCO, R. E. 1977 Coherent motions in the outer region of turbulent boundary layers. *Phys. Fluids* **20**, S124.

FALCO, R. E. 1980 The production of turbulence near a wall. *AIAA Paper* 80–1356.

KIM, J. 1983 On the structure of wall-bounded turbulent flows. *Phys. Fluids* **26**, 2088.

KIM, J. 1985 Turbulence structures associated with the bursting event. *Phys. Fluids* **28**, 52.

KIM, H. T., KLINE, S. J. & REYNOLDS, W. C. 1971 The production of turbulence near a smooth wall in a turbulent boundary layer. *J. Fluid Mech.* **50**, 133.

KLINE, S. J. 1978 The role of visualization in the study of the structure of the turbulent boundary layer. In *Coherent Structure of Turbulent Boundary Layers* (ed. C. R. Smith & D. E. Abbott), p. 1. AFOSR/Lehigh University Workshop, Dept. Mech. Engng & Mech., Bethlehem, Pa.

KLINE, S. J., REYNOLDS, W. C., SCHRAUB, F. A. & RUNSTADLER, P. W. 1967 The structure of turbulent boundary layers. *J. Fluid Mech.* **30**, 741.

KREPLIN, H. & ECKELMANN, H. 1979 Behavior of the three fluctuating velocity components in the wall region of a turbulent channel flow. *Phys. Fluids* **22**, 1233.

LEONARD, A. 1980 Vortex simulation of three-dimensional spotlike disturbances in a laminar boundary layer. *Turbulent Shear Flows* 2, p. 67. Springer-Verlag.

LU, S. S. & WILLMARTH, W. W. 1973 Measurements of the structure of the Reynolds stress in a turbulent boundary layer. *J. Fluid Mech.* **60**, 481.

MOIN, P. 1984 Probing turbulence via large eddy simulation. *AIAA Paper* 84–0174.

MOIN, P. & KIM, J. 1982 Numerical investigation of turbulent channel flow. *J. Fluid Mech.* **118**, 341.

MOIN, P. & KIM, J. 1985 The structure of the vorticity field in turbulent channel flow. Part 1. Analysis of instantaneous fields and statistical correlations. *J. Fluid Mech.* **155**, 441.

MOSER, R. D. & MOIN, P. 1984 Direct numerical simulation of curved turbulent channel flow. *NASA TM* 85974. Also, *Report TF*-20, Department of Mech. Engng, Stanford Univ., Stanford, Calif.

PRATURI, A. K. & BRODKEY, R. S. 1978 A stereoscopic visual study of coherent structures in turbulent shear flow. *J. Fluid Mech.* **89**, 251.

THEODORSEN, T. 1952 Mechanism of turbulence. In *Proc. 2nd Midwestern Conf. on Fluid Mech.*, Ohio State University, Columbus, Ohio.

WALLACE, J. M., ECKELMANN, H. & BRODKEY, R. S. 1972 The wall region in turbulent shear flow. *J. Fluid Mech.* **54**, 39.

WILLMARTH, W. W. & LU, S. S. 1972 Structure of the Reynolds stress near the wall. *J. Fluid Mech.* **55**, 65.